Applied Thermal Engineering 230 (2023) 120736

Contents lists available at ScienceDirect

Applied Thermal Engineering

journal homepage: www.elsevier.com/locate/ate

Research Paper

Temperature dependence modeling and experimental evaluation of a multidimensional discrete magnetostrictive actuator☆

Long Chen, Yuchuan Zhu *, Jie Ling, Mingming Zhang

The College of Mechanical and Electrical Engineering, Nanjing University of Aeronautics and Astronautics, Nanjing 210016, Jiangsu, China

ARTICLE INFO

Keywords:
Magnetostrictive actuator
Multidimensional discrete configuration
Temperature influence mechanism
Temperature dependence modeling
Experimental validation

ABSTRACT

Active combustion control has shown a bright prospect for suppressing aero-engine combustion oscillations but also puts forward higher requirements for the actuator on the high bandwidth, large stroke, and high weight-power ratio. A multidimensional discrete magnetostrictive actuator proposed in our previous work can meet these requirements simultaneously. However, the temperature of the working environment around the aero-engine is high, so it is essential to further investigate the temperature-dependent characteristics of the actuator. In this paper, a multi-physics coupled temperature-dependent analytical model is developed, and the influence mechanism of temperature on the actuator is analyzed from the perspective of physics with a wide field of view from the material level to the actuator system level. Experiments based on a fabricated prototype were conducted and the results indicate that both the stroke, hysteresis, and closed-loop tracking performance of the actuator decrease with the increase in temperature, but the temperature has little effect on the frequency response; the proposed analytical model can accurately describe the temperature-dependent output characteristics of the multidimensional discrete magnetostrictive actuator, the root mean square error of which is less than 3% within 200 Hz.

1. Introduction

To improve combustion efficiency and reduce the pollutant emissions of aero-engines, lean combustion technology [1,2] has been widely used in civil aviation [3]. However, it also brings combustion instability embodied in pressure oscillations of the combustion chamber [4–6], which will seriously endanger the safety of the aircraft [7,8]. To suppress these combustion oscillations, based on the characteristics of high efficiency and wide adaptability, active combustion control (ACC) has become a hot research topic [9,10].

In a traditional ACC system, there are three main subsystems [11–13], i.e., the sensor system that is responsible for pressure fluctuation measurement and needs to be directly exposed to the thousandth-degree Celsius heat of the combustion chamber, the control system, which is in charge of oscillating signal processing and needs to deal with changeable working conditions, and the actuator system which is responsible for real-time adjustment of fuel flow. At present, sensors for pressure and optical measurement with high operating temperatures are commercially available [14], and active control algorithms with strong robustness have also been developed [15–17]. However, the ACC system requires the actuator to have high bandwidth, large stroke, and high energy density at the same time [18,19]. Neither the electromagnetic actuator [20], the traditional smart material actuator [18,21], nor the smart material actuator with displacement amplification mechanism [22,23], none of them can meet these requirements simultaneously.

To address these issues and further promote the application of ACC in aero-engines, a novel multidimensional discrete magnetostrictive actuator (MDMA) was proposed in our previous work [24]. By adopting the multidimensional discrete configuration, a stroke of 100 μm and a working bandwidth exceeding 1000 Hz are achieved simultaneously at a volume of 163.1 cm^3 and a weight of 787 g, which meets the requirements of the ACC system for actuators. However, although actuators do not need to face the heat of the combustion chamber directly like sensors, combined with the working environment around the aero-engine, the operating temperature of actuators is still high. But the output characteristics of MDMA in a high-temperature environment have not yet been investigated. Therefore, to further realize the

☆ This work was supported by: the National Natural Science Foundation of China (Grant No. 51975275), the Primary Research & Development Plan of Jiangsu Province (Grant No. BE2021034), the Fundamental Research Funds for the Central Universities (Grant No. NS2022051), the National Key Laboratory of Science and Technology on Helicopter Transmission (Grant No. HTL-A-22G03), the Postgraduate Research & Practice Innovation Program of Jiangsu Province (Grant No. KYCX21_0195).

* Corresponding author.
E-mail address: meeyczhu@nuaa.edu.cn (Y. Zhu).

https://doi.org/10.1016/j.applthermaleng.2023.120736
Received 15 November 2022; Received in revised form 24 April 2023; Accepted 5 May 2023
Available online 12 May 2023
1359-4311/© 2023 Published by Elsevier Ltd.

application of ACC in aero-engines, it is of great significance to analyze the mechanism of temperature influence on the output performance of MDMA.

Many studies indicate that temperature has a great influence on the properties of magnetostrictive materials. Jin et al. [25] proposed a nonlinear magneto-thermo-elastic coupled hysteretic constitutive model, and Zhan et al. [26] presented a three-dimensional multi-field coupled constitutive model, both are aimed at the prediction of temperature influence on magnetization and nonlinear magnetostrictive strain of the magnetostrictive material Terfenol-D. Through the introduction of temperature-dependent hysteresis parameters, a physical model based on the Jiles–Atherton theory was developed by Raghunathan et al. [27] to study the effects of temperature on the magnetic hysteresis of ferromagnetic materials. To analyze the influence of temperature on the permeability and elastic modulus of magnetostrictive materials, Zhou et al. [28] proposed a magneto-thermo-mechanical coupled constitutive model. To investigate the effects of temperature on the magnetic properties and loss characteristics of magnetostrictive materials, Huang et al. [29] experimentally tested the magnetic characteristics of three different magnetostrictive materials from 10 °C to 80 °C.

Temperature also influences the electrical resistivity, permeability, and elastic modulus of other components. A series of temperature-dependence experiments on the electrical resistivity of metal materials and magnetostrictive materials were carried out by Poker et al. [30] and Cook et al. [31], and the results indicated that the electrical resistivity is linearly positively correlated with the temperature. Homoplastically, the elastic modulus of metal materials such as stainless steel [32] and pure iron [33] will decrease with the increase in temperature, showing a linear negative relationship within 200 °C. On the contrary, there is a nonlinearity between temperature and the relative permeability of metal materials, but the correlation is weak within 400 °C [34,35] which can be ignored.

However, research on the system level temperature dependent characteristics of magnetostrictive actuators has been carried out marginally. Because there is a great obstacle to establishing an analytical model for the temperature dependence of the actuator system based on physics. Cai et al. [36] established an equivalent circuit model to describe the effect of temperature on the resonance frequency of a magnetostrictive ultrasonic transducer. To describe the system level input–output temperature dependence relationships of magnetostrictive devices, Huang et al. [37] proposed an electromagnetic-mechanical-thermal fully coupled nonlinear model with the combination of a finite element model. To avoid the difficulties in analytical modeling methods, which are based on physical mechanism, an online model identification approach is proposed by Yi et al. [38] to describe the temperature dependence of magnetostrictive actuators.

A more difficult factor is that, different from traditional magnetostrictive actuators, the MDMA has a complex structure as well as a complex electro-magneto-elastic-mechanical energy conversion process because of its multidimensional discrete configuration. In our previous work [24], a theoretical model has been established to describe the output characteristics of the MDMA, which includes a magnetic equivalent circuit (MEC) model, a nonlinear dynamic magnetization model, a magnetostrictive force model and a multi-body mechanical dynamic model. However, it is not yet capable of describing the temperature dependence of the MDMA.

In this paper, based on the theoretical model established in our previous work [24], a multi-physics coupled temperature dependent (MCTD) analytical model is proposed to investigate the mechanism of temperature influence on the output characteristics of the MDMA. In which, the magneto-thermo-elastic dependence of magnetic resistance is considered in the magnetic equivalent circuit (MEC) model, the temperature dependent resistivity and temperature dependent magnetization process of magnetostrictive materials are considered in the nonlinear dynamic magnetization model, and the magneto-thermo-elastic dependent elasticity modulus is considered in the magnetostrictive force model and multi-body mechanical dynamic model. Then a prototype of the MDMA was fabricated and a series of experiments were carried out to investigate the influence of temperature on its open-loop and closed-loop performance. The results indicate that, both the output displacement and hysteresis of the MDMA decrease gradually with the increase in temperature, the degree of which are about 12% and 27% at 70 °C respectively; but the temperature has a little effect on the frequency response of MDMA; the temperature has a certain effect on the closed-loop displacement tracking performance of the MDMA, the tracking error will increase under high working temperature; the proposed MCTD model can describe the temperature dependent output characteristics of the MDMA accurately, the root mean square error of which is less than 3% within 200 Hz and about 7% at 400 Hz.

The remainder of this paper is structured as follows: The structure and temperature influence mechanism analysis of the MDMA is shown in Section 2. In Section 3, the MCTD analytical model was established with the consideration of the magneto-thermo-elastic coupling between the constitutive relation of magnetostrictive materials and the structural dynamics in the MDMA. The temperature-dependent experiments on a fabricated prototype of the MDMA and the accuracy verification for the proposed MCTD analytical model are carried out in Section 4. In Section 5, a series of analyses based on the proposed MCTD analytical model are carried out. Section 6 gives the conclusions.

2. Structure and temperature influence mechanism of the MDMA

2.1. Structure and working principle

As shown in Fig. 1, the MDMA can be divided into three parts, i.e., the magnetostrictive stack, the electromagnetic excitation section, and the preload application mechanism. To achieve both high bandwidth and large stroke in a confined volume, the multidimensional discrete configuration [24] is employed by MDMA. The magnetostrictive stack consists of three magnetostrictive rods that are nested in the radial direction through the employment of two sleeves and four magnetizers, and each magnetostrictive rod consists of four short rods axially. The axial dispersion maintains high bandwidth, and the radial dispersion realizes displacement amplification. In the electromagnetic excitation section that contains coils and permanent magnets, the excitation coil is separated into four parts with uniform axial distribution to improve bandwidth, the permanent magnets are employed to provide bias magnetic field and eliminate the frequency doubling effect [39]. The innermost layer of each excitation coil unit has an induction coil, which is responsible for sensing the magnetic flux density. For the preload application mechanism, which consists of discrete disk springs in series, the preload can be adjusted by rotating the end cover.

In the working process of the MDMA, the current passes through the excitation coil to generate a control magnetic field, which magnetizes the magnetostrictive stack together with the permanent magnets' bias magnetic field. After being magnetized, all the magnetostrictive rods deform simultaneously to produce magnetostrictive strain then the magnetostrictive force and output their displacement along the axial direction. The sleeve transmits the displacement of the outer tubular magnetostrictive rod radially inward, and finally converges to the top of the innermost cylindrical magnetostrictive rod, which becomes the total output displacement of the magnetostrictive stack.

2.2. Temperature influence mechanism

The influence of temperature on the actuator's output characteristics is a macroscopic reflection of the temperature dependence of material parameters. Therefore, the temperature influence mechanism of MDMA can be summarized in Fig. 2, which includes the following three levels.

The first is the material level. According to the structure and working process of MDMA, the temperature dependence of the magnetic permeability, electrical resistivity, saturated magnetization, and elastic modulus of magnetostrictive rods is the most important factor that has

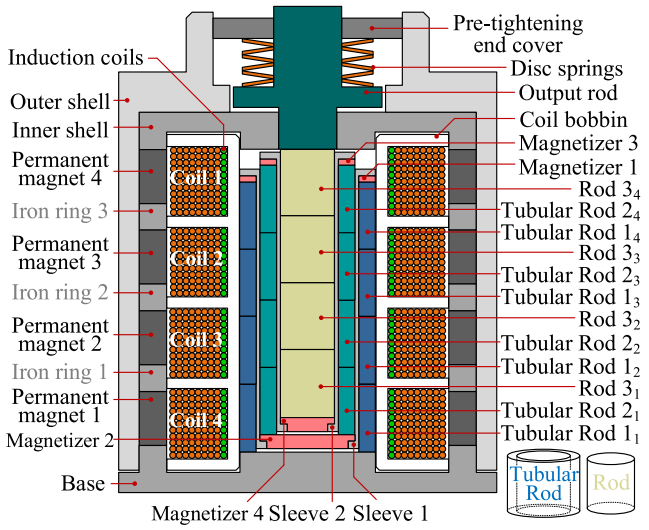

Fig. 1. The structure of the MDMA.

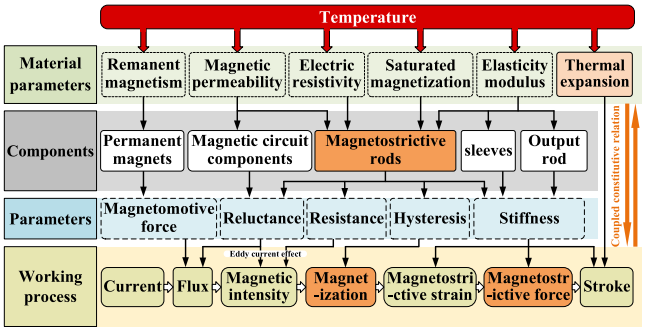

Fig. 2. The mechanism of temperature effect on MDMA.

a crucial influence on the performance of MDMA. The temperature also influences the remanent magnetism of permanent magnets, the magnetic permeability of magnetic circuit components, and the elastic modulus of sleeves. Thermal expansion of each component is also a side effect of temperature.

The second is the actuator system level. The temperature dependent variation of material parameters will lead to changes in the structural parameters of each component, and further affect the electro-magneto-mechanical energy conversion process of the MDMA. For the electro-magnetic conversion processes, the temperature-dependent variation of the remanent magnetism of permanent magnets will result in a change of the bias magnetic field. According to the magnetic circuit theory and eddy current effects, the effective magnetic field intensity will fluctuate due to temperature-dependent changes in the permeability that affect the reluctance and the resistivity that affect the resistance. For the magneto-mechanical conversion process, the variation of the saturated magnetization and the elastic modulus will change the stiffness of magnetostrictive rods and sleeves, which has a great impact on the performance of MDMA.

The third is that the effect of temperature on the MDMA is not unidirectional but multi-physics coupled. Magneto-thermal-elastic-mechanical coupling exists at both the magnetostrictive material level and the actuator system level.

3. Temperature-dependent analytical modeling of the MDMA

Considering the magneto-thermo-elastic dependence of the magnetic permeability, the resistivity, the magnetization, and the elastic modulus of each component, a multi-physics coupled temperature dependence (MCTD) analytical model is established in this section based on the theoretical model proposed in our previous work [24].

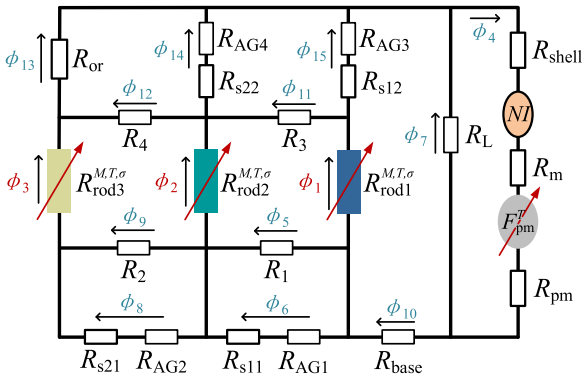

Fig. 3. The proposed temperature-dependent magnetic equivalent circuit model.

Table 1
The parameters of the MEC model.

Symbol	Value (H^{-1})	Symbol	Value (H^{-1})
R_{shell}	5.34×10^{3}	R_1	1.81×10^{7}
R_{base}	5.23×10^{3}	R_2	2.34×10^{7}
R_{or}	1.50×10^{3}	R_3	4.11×10^{6}
R_{s11}	865.4	R_4	3.20×10^{6}
R_{s12}	484.6	R_{AG1}	2.25×10^{6}
R_{s21}	2.65×10^{3}	R_{AG2}	6.25×10^{6}
R_{s22}	737.5	R_{AG3}	2.37×10^{7}
R_m	1.39×10^{3}	R_{AG4}	7.40×10^{8}
R_L	9.13×10^{8}	R_{pm}	1.88×10^{6}

3.1. Temperature-dependent magnetic equivalent circuit model

To describe the uneven magnetic field distribution of the MDMA, a magnetic equivalent circuit model was proposed in our previous work [24,40]. On the base of which, with the consideration of coupled thermal effects on the magnetic circuit components and permanent magnets, a temperature-dependent magnetic equivalent circuit (TDMEC) model was established as shown in Fig. 3, where F^T_{pm} is the temperature dependent bias magnetomotive force of the permanent magnets; $R^{M,T,\sigma}_{rod1}$, $R^{M,T,\sigma}_{rod2}$ and $R^{M,T,\sigma}_{rod3}$ represents the magneto-thermo-elastic dependent magnetic reluctance of rod 1, rod 2 and rod 3 respectively. For the key magnetic circuit components made of pure iron, such as the inner shell, the base, the output rod, and the magnetizers, their parameters have been obtained in our previous work, as shown in Table 1. Because the temperature dependence of the relative permeability of pure iron is weak [34,35,41] within 400 °C, their temperature dependence is ignored. For other components made of non-magnetic materials, air, and permanent magnets with excellent temperature stability, their relative permeability hardly changes with temperature.

According to Kirchhoff's law, the TDMEC model can be described by (23) in Appendix A, in which ϕ_1, ϕ_2 and ϕ_3 are the magnetic flux of each magnetostrictive rod that needs to be solved. For the temperature-dependent bias magnetomotive force F^T_{pm}, which can be calculated as [42]:

$$F^T_{pm} = F_{pm}(1+\alpha_{pm1}(T-T_0)+\alpha_{pm2}(T-T_0)^2) \quad (1)$$

where F_{pm} is the original bias magnetomotive force; T is the operating temperature; T_0 represents the original temperature, in this paper is 20 °C; α_{pm1} and α_{pm2} are the temperature coefficients. For the magneto-thermo-elastic dependent magnetic resistance of each magnetostrictive

rod, which can be calculated numerically through:

$$R_{\mathrm{rod}}^{M,T,\sigma} = \frac{l_{\mathrm{G}}^{T}}{\mu_{\mathrm{G}}^{M,T,\sigma} A_{\mathrm{G}}^{T}} \tag{2}$$

where l_{G}^{T} and A_{G}^{T} are the temperature-dependent length and cross-sectional area of the magnetostrictive rod according to the thermal expansion effect, respectively; $\mu_{\mathrm{G}}^{M,T,\sigma}$ is the magneto-thermo-elastic dependent magnetic permeability of magnetostrictive rods which can be obtained as [28]:

$$\mu_{\mathrm{G}}^{M,T,\sigma} = \mu_0 \left[1 + \left(\frac{\pi}{2kM_s^T} \sec^2\left(\frac{\pi M}{2M_{\mathrm{s}}^T}\right) - \frac{2(\lambda_{\mathrm{s}}\sigma - \Lambda_0(\sigma))}{\mu_0 (M_{\mathrm{s}}^T)^2} - \frac{2\beta \Delta T \sigma}{\mu_0 (M_{\mathrm{s}}^T)^2} \right)^{-1} \right] \tag{3}$$

where μ_0 is the vacuum permeability; M is the magnetization intensity; λ_{s} is the saturation magnetostrictive strain; σ is the stress of magnetostrictive material; β is the linear variation coefficient; ΔT represents the temperature increment; M_{s}^T is the temperature-dependent saturation magnetization, which can be expressed as follow [27,28]:

$$M_{\mathrm{s}}^T = M_{\mathrm{s}} \left(1 - \frac{\Delta T}{T_{\mathrm{c}} - T_{\mathrm{r}}}\right)^{x} \tag{4}$$

where T_{c} is the Curie temperature; T_{r} is the room temperature, i.e., 20 °C; M_{s} is the saturation magnetization of the room temperature; x is the amplification coefficient that reflects the slope of the change in saturation magnetization with temperature. k is the relaxation factor which can be calculated as [28]:

$$k = \frac{\pi}{2} \frac{\chi_{\mathrm{m}}}{M_{\mathrm{s}}^T} \tag{5}$$

where χ_{m} is the initial magnetic susceptibility of the magnetization curve at $T = T_{\mathrm{r}}$ for a free state.

$\Lambda_0(\sigma)$ is the original function of the elastic strain $\lambda_0(\sigma)$ that is related to magnetic domain rotation which can be expressed as follow [28]:

$$\Lambda_0(\sigma) = \frac{\lambda_{\mathrm{s}}\sigma}{4} + \frac{3\lambda_{\mathrm{s}}\sigma_\lambda}{4} \ln\left[\frac{2\sqrt{2}}{3} \cosh\frac{(\sigma - \sigma_0)}{\sigma_\lambda} \right] \tag{6}$$

where σ_λ is the magnetic domain rotation saturation stress; the constant $\sigma_0 = \sigma_\lambda \operatorname{arctanh}(1/3)$.

3.2. Temperature-dependent nonlinear dynamic magnetization model

The excitation coil generates a magnetic field under which the magnetostrictive material will be magnetized. Temperature has a significant effect on both processes.

With the consideration of temperature-dependent magnetic permeability and resistivity as shown in Fig. 4, considering the eddy current effect, the magnetic field intensity of the magnetostrictive rod can be calculated as [24]:

$$\begin{cases} H = H_{\mathrm{c}} - H' = \dfrac{\phi}{k_{\mathrm{f}} \mu_{\mathrm{G}}^{M,T,\sigma} A_{\mathrm{G}}^{T}} - \displaystyle\int_{r_2^T}^{r_1^T} r \mathrm{d}r \frac{\mu_{\mathrm{G}}^{M,T,\sigma}}{2k_{\mathrm{J}}\rho_{\mathrm{G}}^{T}} \frac{\mathrm{d}H_{\mathrm{c}}}{\mathrm{d}t} \\ H(s) = \dfrac{\phi}{k_{\mathrm{f}} \mu_{\mathrm{G}}^{M,T,\sigma} A_{\mathrm{G}}^{T} (1 + \mu_{\mathrm{G}}^{M,T,\sigma} ((r_1^T)^2 - (r_2^T)^2) s / 4k_{\mathrm{J}}\rho_{\mathrm{G}}^{T})} \end{cases} \tag{7}$$

where H_{c} is the magnetic field intensity; H' is the magnetic intensity generated by the eddy current; ϕ is the magnetic flux which can be calculated by Eq. (23); $\mu_{\mathrm{G}}^{M,T,\sigma}$ is the magneto-thermo-elastic dependent magnetic permeability of the magnetostrictive rod; r_1^T and r_2^T is the temperature-dependent outer and inner radius of a magnetostrictive rod respectively; k_{f} and k_{J} are the magnetic flux leakage compensation factor and the eddy current effect compensation factor, respectively; ρ_{G}^{T} is the temperature-dependent resistivity of the magnetostrictive rods can be calculated as [31]:

$$\rho_{\mathrm{G}}^{T} = \rho_{\mathrm{G}} + 2.5 \times 10^{-9} (T - T_0). \tag{8}$$

Magnetostrictive materials will be magnetized under the excitation of an external magnetic field. The Jiles–Atherton model is the most widely used magnetization model that can describe the temperature-dependent magnetization process of a magnetostrictive rod as follows [27,43]:

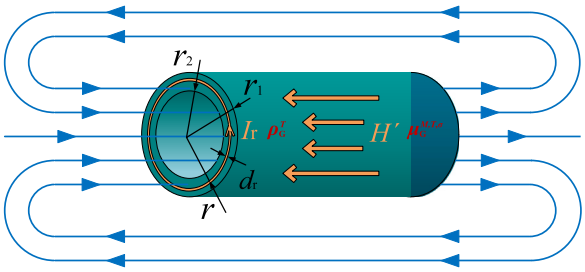

Fig. 4. The eddy current at radius r.

$$\begin{cases} H_{\mathrm{e}} = H + \alpha^T M \\ M_{\mathrm{ir}} = M_{\mathrm{an}} - k^T \delta \left(\dfrac{\mathrm{d}M_{\mathrm{ir}}}{\mathrm{d}H_{\mathrm{e}}}\right) \\ M = M_{\mathrm{r}} + M_{\mathrm{ir}} \\ M_{\mathrm{an}} = M_{\mathrm{s}}^T \left[\coth\left(\dfrac{H_{\mathrm{e}}}{a^T}\right) - \dfrac{a^T}{H_{\mathrm{e}}}\right] \\ M_{\mathrm{r}} = c^T (M_{\mathrm{an}} - M_{\mathrm{ir}}) \end{cases} \tag{9}$$

where M is the magnetization intensity; M_{s}^T is the temperature dependent saturation magnetization; H_{e} is the effective magnetic field; M_{r} is the reversible value of magnetization; M_{ir} is the temperature dependent magnetization's irreversible value; M_{an} is a hysteretic value of magnetization; δ is the directional coefficient; α^T is the temperature dependent magnetic domain interaction coefficient that depicts the relation between the prestress and magnetic domain; k^T is the temperature dependent pinning coefficient (the characteristic coefficient of hysteresis); a^T is the temperature dependent shape coefficient of the magnetization curve without hysteresis and c^T is the temperature dependent reversible coefficient. The temperature dependence of the above parameters can be expressed as follows [27]:

$$\begin{cases} \alpha^T = \alpha_0 e^{-\frac{2}{\beta_1}\frac{T}{T_{\mathrm{c}}}} \left(1 - \dfrac{T}{T_{\mathrm{c}}}\right)^{-\beta_1} \\ k^T = k_0 e^{-\frac{1}{\beta_2}\frac{T}{T_{\mathrm{c}}}} \\ a^T = a_0 e^{-\frac{1}{\beta_3}\frac{T}{T_{\mathrm{c}}}} \\ c^T = c_0 e^{-\frac{2}{\beta_1}\frac{T}{T_{\mathrm{c}}}} \left(1 - \dfrac{T}{T_{\mathrm{c}}}\right)^{-\beta_1} \end{cases} \tag{10}$$

where α_0 is the original magnetic domain interaction coefficient; k_0 is the original pinning coefficient; a_0 is the original shape coefficient; c_0 is the original reversible coefficient; β_1 is the material-dependent critical exponent; β_2 is the critical exponent for pinning constant and β_3 is the critical exponent for domain density.

3.3. Temperature-dependent magnetostrictive force model

The magnetic domain of the magnetostrictive rod will deflect after being magnetized, resulting in magnetostrictive strain and then magnetostrictive force. Based on the magnetostrictive force model in [24], the temperature-dependent saturation magnetization and magneto-thermo-elastic elastic modulus are introduced to describe the influence of temperature on the process. The magnetostrictive strain of each rod can be calculated as follows [39,44]:

$$\lambda = \begin{cases} (1 + \dfrac{1}{2}\tanh\dfrac{2\sigma_{\mathrm{p}}}{\sigma_{\mathrm{s}}}) \lambda_{\mathrm{s}} \dfrac{M^2}{(M_{\mathrm{s}}^T)^2}, & \sigma_{\mathrm{p}} \le \sigma_{\mathrm{s}} \\ (1 - \dfrac{\sigma_{\mathrm{p}} - \sigma_{\mathrm{s}}}{\sigma_{\max}})(1 + \dfrac{1}{2}\tanh\dfrac{2\sigma_{\mathrm{p}}}{\sigma_{\mathrm{s}}}) \lambda_{\mathrm{s}} \dfrac{M^2}{(M_{\mathrm{s}}^T)^2}, & \sigma_{\mathrm{p}} > \sigma_{\mathrm{s}} \end{cases} \tag{11}$$

where λ is the magnetostrictive strain; λ_{s} is the saturation magnetostrictive strain; σ_{p} is the prestress; M_{s}^T is the temperature dependent

saturation magnetization; σ_s and σ_{max} are the saturation and maximum magnetostrictive stress respectively, for each magnetostrictive rod which can be calculated as follows [39]:

$$\begin{cases} \sigma_s = \frac{1}{2}\lambda_s E_G^{M,T,\sigma} \\ \sigma_{max} = \frac{3}{2}\lambda_s E_G^{M,T,\sigma} \end{cases} \tag{12}$$

where $E_G^{M,T,\sigma}$ is the magneto-thermo-elastic dependent elastic modulus of each magnetostrictive rod which can be expressed as [28]:

$$E_G^{M,T,\sigma} = \left[\frac{1}{E_G} + \frac{3\lambda_s}{4\sigma_\lambda}\mathrm{sech}^2\left(\frac{\sigma-\sigma_0}{\sigma_\lambda}\right)\left(1-\frac{M^2}{(M_s^T)^2}\right) + \frac{\left[\frac{3\lambda_s}{2}\left(1-\tanh\left(\frac{\sigma-\sigma_0}{\sigma_\lambda}\right)\right)+2\beta\Delta T\right]^2 \frac{M^2}{(M_s^T)^2}}{\left[\frac{\mu_0\pi M_s^T}{2k}\sec^2\left(\frac{\pi M}{2M_s^T}\right) - 2(\lambda_s\sigma - \Lambda_0(\sigma)) - 2\beta\Delta T\sigma\right]} \right]^{-1}. \tag{13}$$

With the consideration of the coupled magneto-thermo-elastic dependence of elastic modulus of magnetostrictive materials [45], the magnetostrictive force F of each magnetostrictive rod can be calculated as follow [46]:

$$F = \lambda E_G^{M,T,\sigma} A_G^T. \tag{14}$$

3.4. Temperature-dependent multi-body mechanical dynamic model

The magnetostrictive stack of MDMA consists of magnetostrictive rods sleeves and magnetizers. A multi-degree-of-freedom dynamic model has been proposed in [40] to describe their mechanical dynamic characteristics. Temperature affects both the stiffness and damping of the dynamic system. But the temperature dependence of sleeve material and magnetostrictive rod material on damping is weak. The experiments on the frequency characteristics also show that temperature has little effect on the frequency and amplitude of the first-order resonant point of MDMA, which is determined by the damping. So, the influence of temperature on damping is ignored. With the consideration of the temperature-dependent elastic modulus, i.e., stiffness, a temperature-dependent multi-body dynamic model is established furtherly as shown in Fig. 5. The magnetostrictive rods are force sources. Sleeves, magnetizers, and the output rod are transmitters to transfer force and displacement. The dynamic equation can be expressed as follow:

$$\boldsymbol{M}\ddot{\boldsymbol{X}} + \boldsymbol{C}\dot{\boldsymbol{X}} + \boldsymbol{K}^{M,T,\sigma}\boldsymbol{X} = \boldsymbol{F} \tag{15}$$

where $\boldsymbol{M}$, $\boldsymbol{C}$, $\boldsymbol{X}$ and $\boldsymbol{F}$ are the mass matrix, the damping matrix, the displacement matrix and input force matrix respectively, which can be expressed as (24), (25) and (26) in Appendix B; $\boldsymbol{K}^{M,T,\sigma}$ is the magneto-thermo-elastic dependent stiffness matrix, which can be expressed as:

$$\boldsymbol{K}^{M,T,\sigma} = \begin{bmatrix} k_1^{M,T,\sigma} + k_{lr1}^{M,T,\sigma} & 0 & 0 \\ 0 & k_2^{M,T,\sigma} + k_{lr2}^{M,T,\sigma} & 0 \\ 0 & 0 & k_3^{M,T,\sigma} + k_{lr3} \end{bmatrix} \tag{16}$$

where $k_1^{M,T,\sigma}$, $k_2^{M,T,\sigma}$ and $k_3^{M,T,\sigma}$ are the magneto-thermo-elastic dependent stiffness of rod 1, rod 2 and rod 3 respectively, which can be calculated as:

$$k^{M,T,\sigma} = \frac{E_G^{M,T,\sigma} A_G^T}{l_G^T}. \tag{17}$$

$k_{lr1}^{M,T,\sigma}$ and $k_{lr2}^{M,T,\sigma}$ are the magneto-thermo-elastic dependent equivalent load stiffness of rod 1 and rod 2 respectively; k_{lr3} is the equivalent load stiffness of rod 3. Which can be calculated as:

$$\begin{cases} k_{lr1}^{M,T,\sigma} = \left(\frac{1}{k_{M1}} + \frac{1}{k_{t1}^T} + \frac{1}{k_{M2}} + \frac{1}{k_2^{M,T,\sigma}} + \frac{1}{k_{M3}} + \frac{1}{k_{t2}^T} + \frac{1}{k_{M4}} + \frac{1}{k_3^{M,T,\sigma}} + \frac{1}{k_s} + \frac{1}{k_{dh}}\right)^{-1} \\ k_{lr2}^{M,T,\sigma} = \left(\frac{1}{k_{M3}} + \frac{1}{k_{t2}^T} + \frac{1}{k_{M4}} + \frac{1}{k_3^{M,T,\sigma}} + \frac{1}{k_s} + \frac{1}{k_{dh}}\right)^{-1} \\ k_{lr3} = \left(\frac{1}{k_s} + \frac{1}{k_{dh}}\right)^{-1} \end{cases} \tag{18}$$

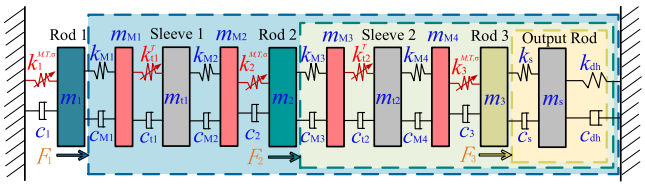

Fig. 5. Schematic of the temperature-dependent multi-body mechanical dynamic model.

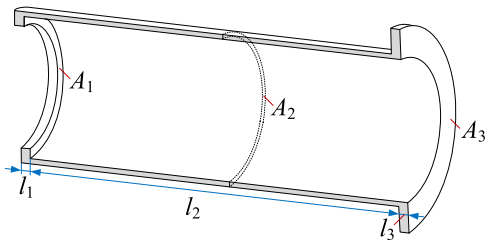

Fig. 6. The key dimensions of the sleeve.

where k_{M1}, k_{M2}, k_{M3}, k_{M4}, k_s and k_{dh} are the stiffness of magnetizer 1, magnetizer 2, magnetizer 3, magnetizer 4, output rod and disk spring respectively; k_{t1}^T and k_{t2}^T are the temperature dependent stiffness of sleeve 1 and sleeve 2 respectively, which can be expressed as:

$$k_t^T = \left(\frac{l_1^T}{E_t^T A_1^T} + \frac{l_2^T}{E_t^T A_2^T} + \frac{l_3^T}{E_t^T A_3^T}\right)^{-1} \tag{19}$$

where E_t^T is the temperature-dependent elasticity modulus of sleeves, according to the function of temperature dependent elasticity modulus of stainless steels [32] which can be expressed as $E_t^T = E_t - 0.10667T$ and the unit of E_t and T are GPa and °C respectively; l_1^T to l_3^T and A_1^T to A_3^T are the temperature-dependent length and the cross-sectional area of the sleeve according to the thermal expansion effect as shown in Fig. 6. Finally, the state space model of the dynamic system can be established as follows [40]:

$$\begin{cases} \begin{bmatrix} \dot{\boldsymbol{X}} \\ \ddot{\boldsymbol{X}} \end{bmatrix} = \begin{bmatrix} \boldsymbol{0} & \boldsymbol{1} \\ -\boldsymbol{M}^{-1}\boldsymbol{K}^{M,T,\sigma} & -\boldsymbol{M}^{-1}\boldsymbol{C} \end{bmatrix} \begin{bmatrix} \boldsymbol{X} \\ \dot{\boldsymbol{X}} \end{bmatrix} + \begin{bmatrix} \boldsymbol{0} \\ \boldsymbol{M}^{-1} \end{bmatrix} \boldsymbol{F} \\ \boldsymbol{Y} = \begin{bmatrix} \boldsymbol{1} & \boldsymbol{0} \end{bmatrix} \begin{bmatrix} \boldsymbol{X} \\ \dot{\boldsymbol{X}} \end{bmatrix}. \end{cases} \tag{20}$$

3.5. Thermal expansion model

Under high temperatures, each component of the MDMA will generate thermal expansion that is linear with temperature increments. But some of whose expansion has a positive effect on the compensation of thermal displacement. As shown in Fig. 7, because the upper end of the sleeve is fixed with the magnetostrictive rod and the lower end is free, the output direction of its thermal displacement is opposite to that of the magnetostrictive stack, which can offset the error caused by the thermal expansion of other components. Therefore, the thermal expansion displacement of the MDMA can be expressed as:

$$x_T = (\alpha_G l_G + \alpha_M l_M + \alpha_s l_s - \alpha_t l_t)\Delta T \tag{21}$$

where α_G, α_M, α_s and α_t are the thermal expansion coefficient of the magnetostrictive rod, magnetizer, output rod, and sleeve respectively; l_G, l_M, l_s and l_t are the length of the magnetostrictive rod, magnetizer, output rod and sleeve at room temperature, respectively.

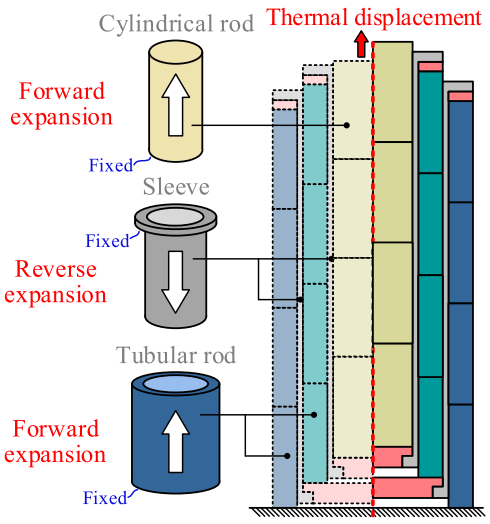

Fig. 7. Thermal expansion of the magnetostrictive stack.

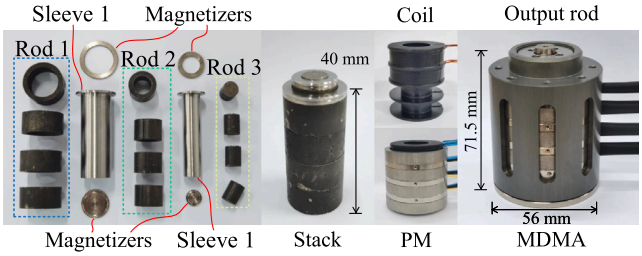

Fig. 8. Prototype of the MDMA.

4. Experimental evaluation

In this section, a prototype of the MDMA was manufactured and a temperature dependence test bench was established, based on which a series of experiments were carried out to evaluate the temperature-dependent performance of the MDMA and verify the accuracy of the MCTD model.

4.1. Prototype of the MDMA

As shown in Fig. 8, a prototype for the MDMA was fabricated with the employment of the magnetostrictive material Terfenol-D, and both magnetostrictive rod 1, rod 2 and rod 3 consist of four short Terfenol-D rods. The radial dimensions of each Terfenol-D rod are shown in Table 2. To meet the requirements of the MDMA at high temperatures, samarium cobalt was chosen as the permanent magnet material, whose Curie temperature can reach 700 °C. The excitation coil is developed with the combination of four independent units, the wire diameter of which is 0.6 mm, and the total number of turns is 180 × 4. The Induction coils also have four independent units, the wire diameter of which is 0.5 mm, and the total number of turns is 18 × 4. The coil bobbin is made of polyether-ether-ketone (PEEK) with an operating temperature of 250 °C. The magnetizer material is DT4C, and the sleeve material is SUS304.

4.2. Temperature experimental platform

The temperature dependence experimental platform was developed as shown in Fig. 9, which consists of the temperature control system, the power system, and the signal acquisition and transmitting system. In the temperature control system, a heat chamber is developed. Two

Table 2
The diameter of Terfenol-D rods.

Name	Outer diameter (mm)	Inner diameter (mm)
Rod 1	20	15
Rod 2	14	9
Rod 3	8	–

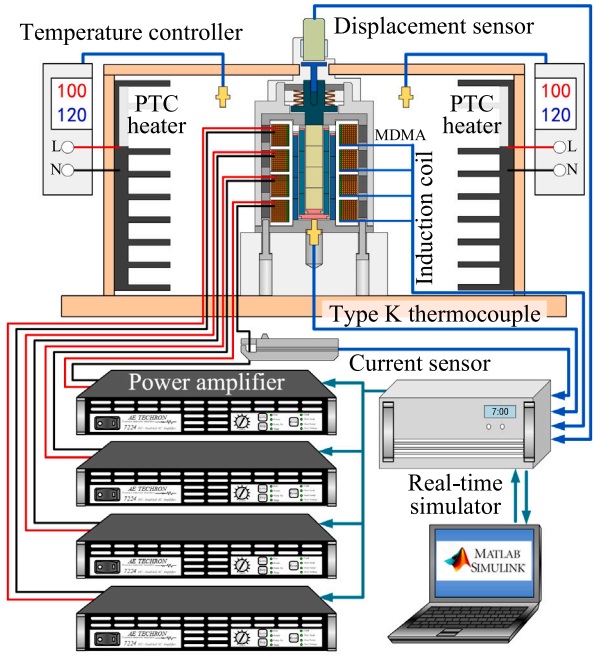

(a) Signal flow diagram

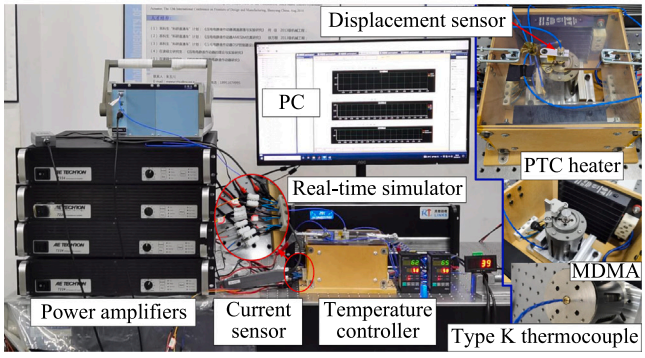

(b) Composition of test bench

Fig. 9. Temperature dependence experimental platform.

PTC heaters (ENMG, CSH3B-2150K) are arranged on both sides of the MDMA, and the ambient temperature inside the heat chamber is controlled by the PID temperature controller (Chang zhou Gaoqi Electronics Co., LTD, XMT5-8201K02-R4) with the employment of the Type K thermocouple as the temperature sensor. In the power system, four power amplifiers (AETechron Inc, 7224) are employed to drive discrete coils of the MDMA, respectively. In the signal acquisition and transmitting system, another Type K thermocouple is installed inside the base to obtain the actual internal temperature of the MDMA. A current sensor (Shenzhen Zhiyong Co., Ltd, CP800) is used to measure the excitation current and the output displacement is acquired by a capacitive displacement sensor (Harbin Core Tomorrow Technology Co., Ltd, E09.Cap). A real-time simulator (Beijing Lingsi Chuangqi

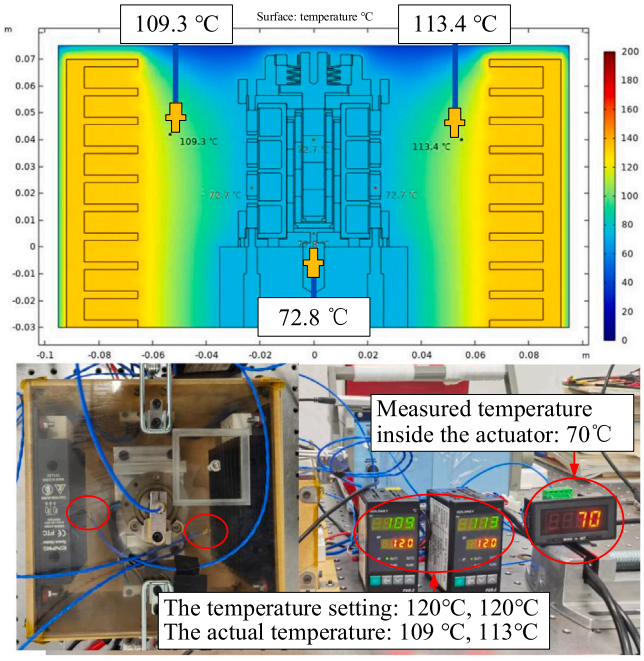

Fig. 10. The Heating system analysis.

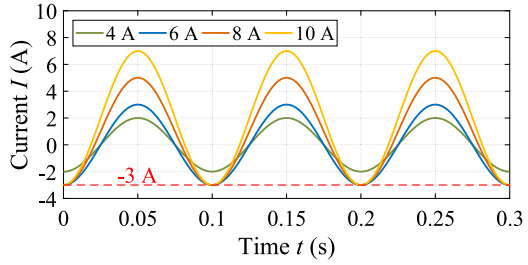

Fig. 11. The excitation signal for the MDMA.

Technology Co., LTD, Links-Box-03) is responsible for excitation signal generation and data acquisition.

4.3. Heating system performance analysis

To evaluate the performance of the temperature control system, a finite element model was developed in COMSOL and an experimental test was carried out. The steady-state result of the temperature distribution in the heat chamber is shown in Fig. 10. The comparison between the simulation result and the experimental result indicates that: (1) The temperature measured by three temperature sensors in the experiment is consistent with the finite element simulation; (2) The internal temperature distribution of the MDMA is uniform and the temperature sensor which was located inside the bottom of the actuator can monitoring the temperature of MDMA accurately. (3) The heat chamber enables the actuator to reach a maximum temperature of 70 °C.

4.4. Temperature dependence investigation

In this subsection, the influence of temperature on the flux density, the output displacement, the hysteresis, the frequency response and the closed-loop displacement tracking performance of the MDMA was investigated at the temperature range from 20 °C to 70 °C (the actual temperature inside the MDMA) though experiment. The bias magnetic field and the thermal expansion of the MDMA were also tested. Due to the coil heating and eddy current effect, the actuator itself will release a lot of heat and cause the temperature to rise during its operation. To minimize the influence of this heat on the accuracy of temperature control, the continuous working time of the actuator was limited to within 0.4 s.

Table 3
The thermal expansivity of MDMA components.

Components	Material	Value (μm/°C × m)
Magnetostrictive rod	Terfenol-D	12.9
Magnetizer	DT4C	12.2
Output rod	DT4C	12.2
Sleeve	SUS304	17.2

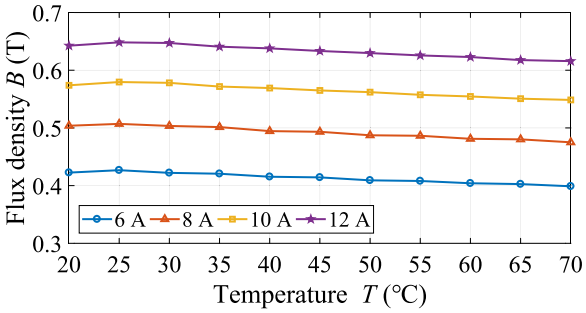

Fig. 12. Effect of temperature on the flux density at 10 Hz.

4.4.1. The bias magnetic field

A bias magnetic field must be applied to eliminate the inherent frequency doubling effect of magnetostrictive materials, which is partly supplied by permanent magnets in the MDMA. The experimental results indicated that the bias magnetic field provided by the permanent magnets is equivalent to the magnetic field generated by the coil at the excitation current of 3.5 A, i.e. the bias magnetomotive force F_{pm} of permanent magnets can be calculated as:

$$F_{pm} = 3.5 \times N = 3.5 \times 720 = 2520 \text{ (At)} \tag{22}$$

where N is the turns of the excitation coil.

Therefore, to prevent the frequency doubling effect, the sinusoidal excitation signal used in the experiment is shown in Fig. 11, the minimum value of which is −3 A, when its peak-to-peak value is greater than 6 A, the coil should be used to provide additional bias magnetic field.

Considering that samarium cobalt permanent magnets possess excellent temperature stability, the remanence temperature coefficient of which is less than 3×10^{-4}, the temperature dependence of bias magnetomotive force can be ignored in the MCTD model.

4.4.2. The thermal expansion

The thermal expansion properties of MDMA were investigated through experiment, and the results indicate that the coefficient of thermal expansion is 0.712 μm/°C. According to the theoretical model in Section 3.5, the thermal expansion coefficient of the MDMA is calculated to be 0.662 μm/°C. The relevant material parameters are shown in Table 3 and according to which, the size change of sleeve and magnetostrictive rod is only about 0.15% between 20-150 °C. Therefore, the temperature dependence of structure sizes can be ignored. In the following experimental tests, the displacement caused by thermal expansion was eliminated.

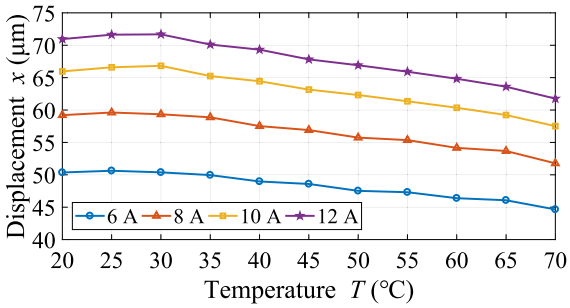

Fig. 13. Effect of temperature on the stroke at 10 Hz.

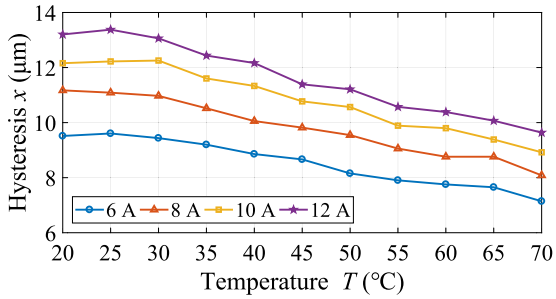

Fig. 14. Effect of temperature on the hysteresis at 10 Hz.

4.4.3. The flux density

The flux density is an important index in the MDMA operation process. The induction coil is used to collect the magnetic flux density during the operation of the actuator in experiments. As shown in Fig. 12, the flux density in MDMA decreases by 5.6%, 5.7%, 4.4% and 4.2% at a temperature rise of 50 °C under the excitation current of 6 A, 8 A, 10 A and 12 A respectively.

4.4.4. The output displacement and hysteresis

Output displacement is one of the most important indexes to evaluate the performance of actuators, the influence of temperature on which was investigated experimentally, the results are shown in Fig. 13. With the temperature increment from 20 °C to 70 °C, the output displacement of the MDMA shrank by 11.3%, 12.6%, 12.8%, and 13.0% under the excitation current of 6 A, 8 A, 10 A, and 12 A, respectively. Therefore, it is necessary to increase the amplitude of the excitation current to compensate for the attenuation of actuator output displacement in high-temperature working environments. The experimental results indicated that temperature has a positive effect on the inhibition of MDMA hysteresis, as shown in Fig. 14. The hysteresis of MDMA was reduced by 25.0%, 27.6%, 26.6% and 27.0% at 70 °C compared with that at 20 °C. Therefore, the linearity of MDMA will be improved with the increase in temperature.

4.4.5. The frequency response

As shown in Fig. 15, the temperature has little effect on the frequency response of MDMA at different temperatures, the first resonant frequency is kept at 1270 Hz, the change of which is less than 0.17% within 70 °C, and the bandwidth exceeds 2000 Hz. Therefore, the MDMA can still meet the requirements of the ACC system for the high operation frequency on the actuator under high temperatures.

4.4.6. The closed-loop tracking performance

In the closed-loop test of the MDMA, the PID controller developed in our previous work [24] is employed, the parameter of which is set as $k_p = 0.2$, $k_i = 0.03$ and $k_d = 0.007$ respectively. The experimental tracking results under different working conditions are shown in

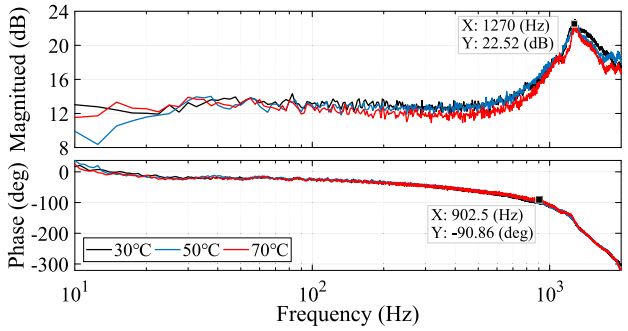

Fig. 15. Effect of temperature on the frequency response.

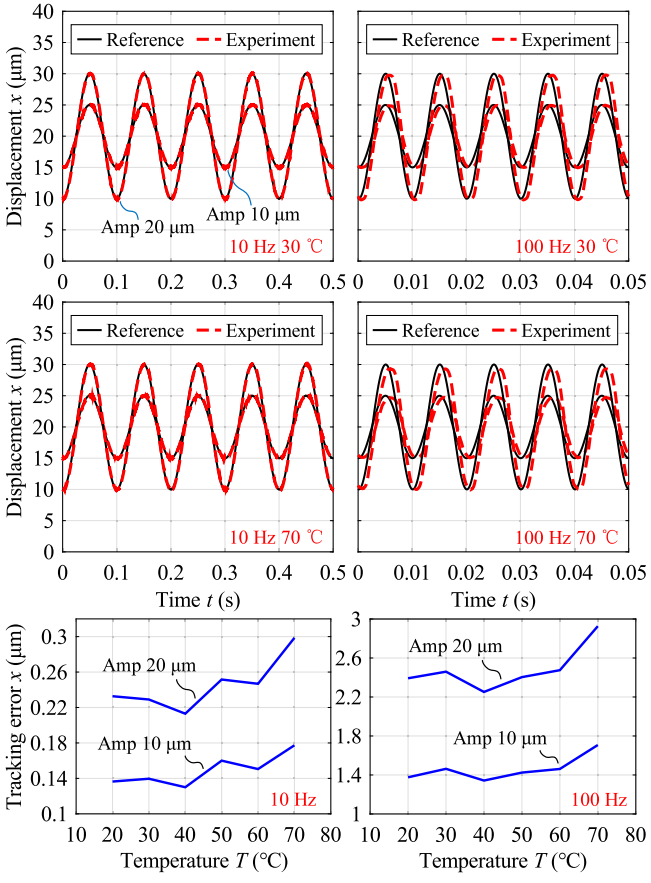

Fig. 16. Effect of temperature on the closed-loop displacement tracking error.

Fig. 16, which indicates that the temperature has a certain effect on the closed-loop tracking performance of MDMA. The tracking error has a minimum point at 40 °C. This is mainly because, below 40 °C, the hysteresis of MDMA decreases more with the increase of temperature than the attenuation of its output displacement, which reduces the nonlinearity of MDMA and makes the displacement tracking error smaller. But with the further increase in temperature, the attenuation of performance becomes more and more serious, and the closed-loop tracking error also increases gradually. Compared with that at 20 °C, the tracking error of the MDMA at 70 °C increases 30%, 28%, 24%, and 22% when the reference displacements are Amp 10 μm 10 Hz, Amp 20 μm 10 Hz, Amp 10 μm 100 Hz and Amp 20 μm 100 Hz respectively.

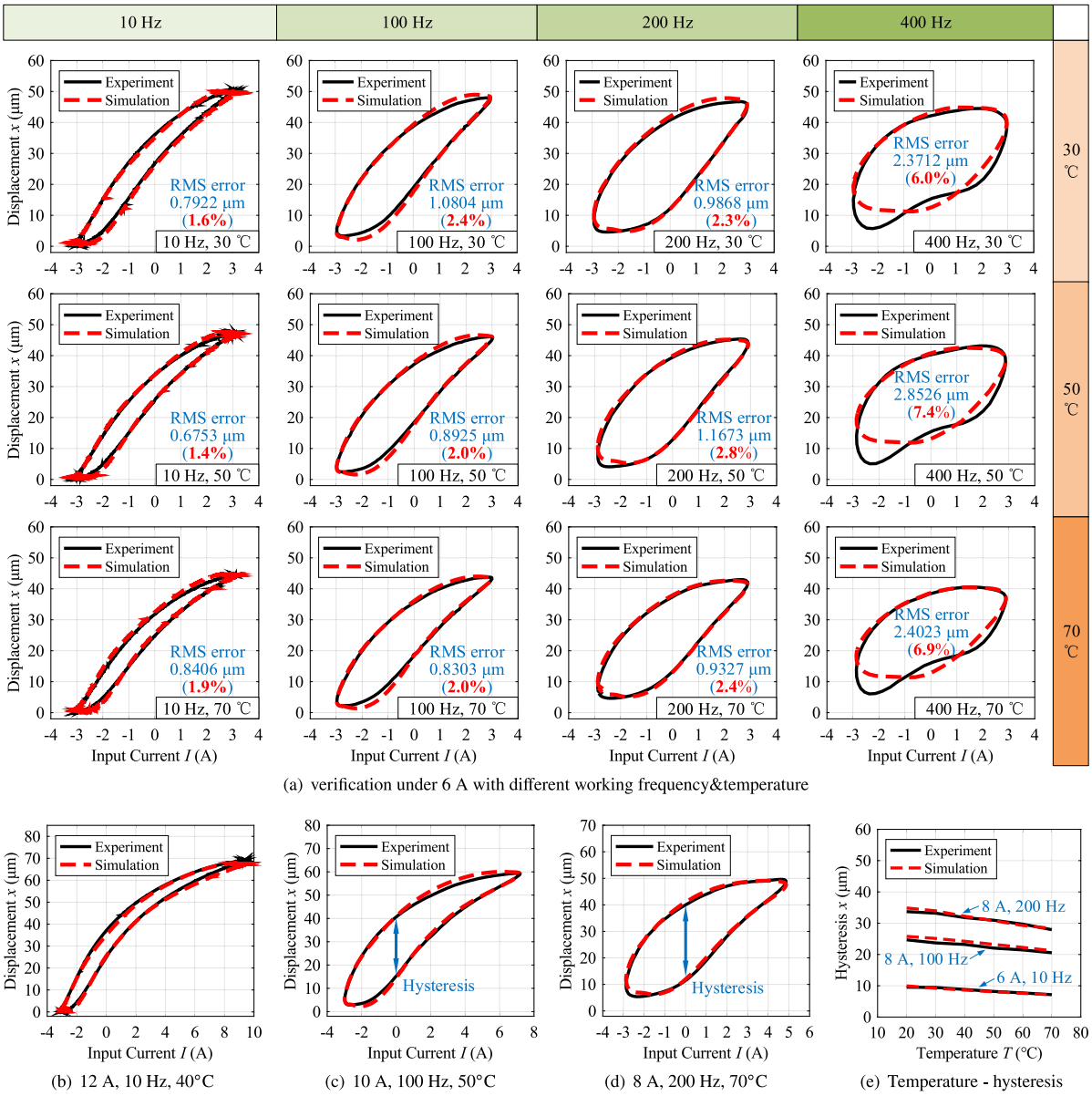

(a) verification under 6 A with different working frequency&temperature

(b) 12 A, 10 Hz, 40°C (c) 10 A, 100 Hz, 50°C (d) 8 A, 200 Hz, 70°C (e) Temperature - hysteresis

Fig. 17. Accuracy verification of the MCTD model.

Table 4
The identified parameters of dynamic magnetization model.

Symbol	Unit	Rod1	Rod2	Rod3
a_0	A m^{-1}	5947	6850	6030
α_0	––	−0.0377	−0.0330	−0.0087
c_0	––	0.0464	0.3962	0.1636
k_0	A m^{-1}	3032	4808	6345
β_1	–	0.6821	0.6085	0.5235
β_2	–	0.3411	0.3043	0.2618
β_3	–	0.3411	0.3043	0.2618
k_f	–	3.80	12.31	3.97
k_J	–	1.07	0.37	0.15

Table 5
The parameters of dynamic model obtained by identification.

Symbol	Unit	Value	Symbol	Unit	Value
c_1	N s m^{-1}	275	c_{t2}	N s m^{-1}	15546
c_{M1}	N s m^{-1}	1304	c_{M4}	N s m^{-1}	3773
c_{t1}	N s m^{-1}	12989	c_3	N s m^{-1}	477
c_{M2}	N s m^{-1}	6580	c_s	N s m^{-1}	1047
c_2	N s m^{-1}	121	c_{dh}	N s m^{-1}	261
c_{M3}	N s m^{-1}	8687	x	–	0.001
β	–	-1.1×10^{-5}	χ_m	–	19.84

4.5. Parameter identification and accuracy verification

In the proposed MCTD model, there is a series of parameters that cannot be acquired through measurement, including a_0, α_0, c_0, k_0, k_J and k_f of Terfenol-D rod 1, rod 2 and rod 3 respectively in the dynamic magnetization model; the damping parameters c_1, c_{M1}, c_{t1}, c_{M2}, c_2, c_{M3}, c_{t2}, c_{M4}, c_3, c_s and c_{dh} in the multi-degree-of-freedom mechanical dynamic model; the parameters x, χ_m, β, β_1, β_2 and β_3 which effect the temperature dependence of the MCTD model, all of them must be identified according to experimental data. To ensure the accuracy of parameter identification and prevent it from falling into the local optimal solution, a multi-island genetic algorithm is employed to perform the identification process. The results of parameter identification are shown in Tables 4 and 5. The other parameters in the MCTD model are shown in Table 6.

Table 6
The parameters in the MCTD model.

Symbol	Unit	Value	Symbol	Unit	Value
m_1	g	38	k_1	N μm^{-1}	137
m_{M1}	g	1.1	k_{M1}	N μm^{-1}	3161
m_{t1}	g	7.1	k_{t1}	N μm^{-1}	156
m_{M2}	g	2.1	k_{M2}	N μm^{-1}	939
m_2	g	25.1	k_2	N μm^{-1}	90
m_{M3}	g	0.72	k_{M3}	N μm^{-1}	2077
m_{t2}	g	4.2	k_{t2}	N μm^{-1}	92
m_{M4}	g	0.62	k_{M4}	N μm^{-1}	506
m_3	g	13.9	k_3	N μm^{-1}	50
m_s	g	7.1	k_s	N μm^{-1}	642
–	–	–	k_{dh}	N μm^{-1}	0.29

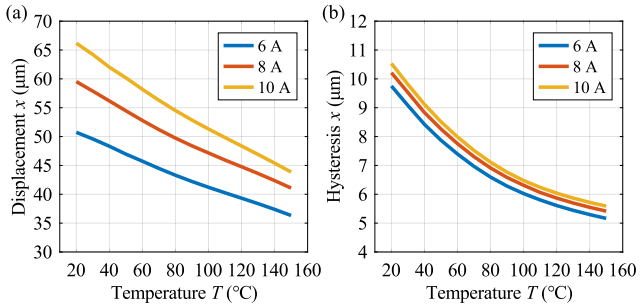

Fig. 18. Simulation results of output displacement and hysteresis of the MDMA at 20–150 °C.

To verify the accuracy of the proposed MCTD model, the comparison between its simulation results and experimental results of the output characteristics of MDMA under different working conditions is shown in Fig. 17, which indicates that the proposed MCTD model can accurately describe the effect of temperature on the input–output characteristics of the MDMA at different working frequencies. The root mean square (RMS) errors of which are less than 3% under low working frequencies and kept around 7% at 400 Hz. The large modeling error at 400 Hz is caused by the lower half distortion of the experimental hysteresis loop. This is mainly due to the displacement sensor itself having certain vibrations under the high frequency excitation of the actuator, which is installed on the actuator's outer shell. We will seek to take the vibration characteristics of the sensor into account in the established model in future work because the actual vibration environment of an aero-engine should be considered in the actuator displacement monitoring and closed-loop control. The Fig. 17(b)–(d) demonstrated that the accuracy of the proposed MCTD model is high and independent of the amplitude of the excitation current. Furthermore, as shown in Fig. 17(e), the hysteresis is extracted as the criterion for the MCTD model's ability on the description of temperature dependence of the MDMA, and the simulation results have a high coincidence with the experiment results under variable temperatures, the maximum error is 0.429 μm (4.5%), 1.424 μm (6.0%) and 1.939 μm (5.3%) under 6 A 10 Hz, 8 A 100 Hz and 8 A 200 Hz respectively.

5. Discussion

According to the active combustion control (ACC) actuator design specifications which were drafted by NASA Glenn Research Center [47], the maximum operating temperature of the ACC actuator is 300°F, i.e., 148.9 °C. But the heat chamber designed in this paper can only allow the actuator to reach a maximum temperature of 70 °C. Moreover, the temperature dependence of each parameter cannot be monitored experimentally. To verify the necessity of considering the temperature dependence of each part of the model and evaluate the performance of MDMA under a wider temperature range, a series of simulation analyses based on the proposed MCTD model were carried out.

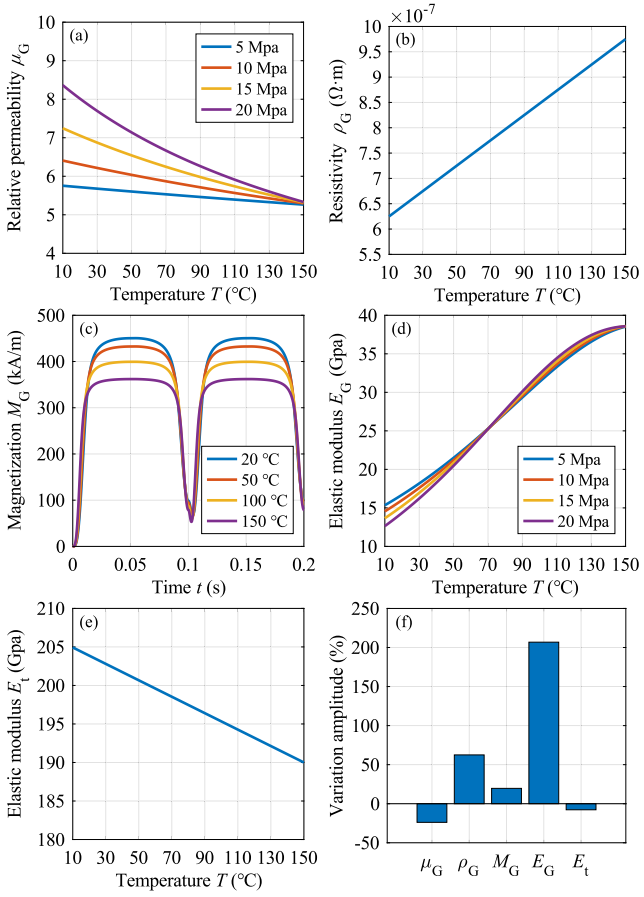

Fig. 19. Temperature dependence of the parameters at 20–150 °C. (a) the magnetostrictive rod's magnetic permeability μ_G, (b) the magnetostrictive rod's resistivity ρ_G, (c) the magnetostrictive rod's magnetization M_G, (d) the magnetostrictive rod's elastic modulus E_G, (e) the sleeve's elastic modulus E_t, (f) variation amplitude of each parameter.

As shown in Fig. 18, the output displacement of the MDMA at 150 °C is about 70% of that at room temperature, which can meet the requirements of ACC on the actuator.

As shown in Fig. 19, the temperature dependence of the magnetostrictive rod's magnetic permeability μ_G, resistivity ρ_G, magnetization M_G, and elastic modulus E_G, as well as the temperature dependence of the sleeve's elastic modulus E_t are analyzed quantitatively. In which E_G has the strongest temperature dependence, it increases by 200% at 150 °C compared to room temperature.

As shown in Fig. 20, the temperature dependence of parameters are ignored respectively to evaluate their contributions to the MCTD model's accuracy independently. And the results under 6 A 10 Hz 70 °C indicated that, at low frequency, if the temperature dependence of the magnetization process is ignored, the error of the MCTD model will increase by 258% from 0.84 μm to 2.17 μm. That is, the temperature dependence of M_G contributes the most to the accuracy of MCTD model, and it has the greatest impact on the high temperature performance of MDMA. In addition, the temperature dependence of E_G and μ_G also nonnegligible, the increase of model error due to the ignorance of which is 226% and 159% respectively.

The results under 6 A 200 Hz 70 °C indicated that, at high frequency, the temperature dependence of resistivity ρ_G and magnetic permeability μ_G contribute the most to the accuracy of the MCTD model, because the eddy current effect increases as the frequency

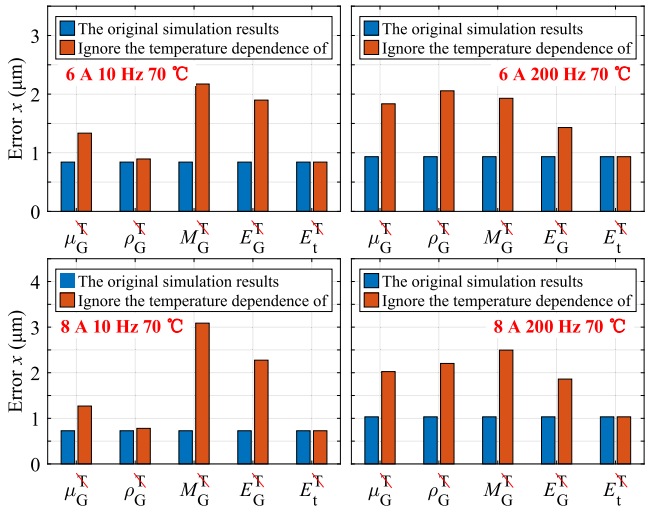

Fig. 20. The error variation of the MCTD model when ignore the temperature dependence of each parameters.

increases, and ρ_G directly determines the intensity of eddy current, μ_G directly affects the strength of the reverse magnetic field generated by the eddy current effect. In addition, the temperature dependence of the elastic modulus E_t has little effect on the high-temperature performance of MDMA. The simulation results under 8 A are consistent with those in 6 A.

6. Conclusion

In this article, for the further application of the multidimensional discrete magnetostrictive actuator in the active combustion control of aero engines, a multi-physics coupled temperature-dependent analytical model is proposed and a series of experiments and simulations are conducted to investigate the influence mechanism of temperature on the actuator's performance. The conclusions are as follows:

(1) The temperature has a negative effect on the output displacement of the multidimensional discrete magnetostrictive actuator, the decrement of which is up to 12% at 70 °C compared with that at 20 °C.
(2) The temperature has a positive effect on the reduction of output hysteresis of the actuator, the degree of which is up to 27% with the temperature increment from 20 °C to 70 °C.
(3) The temperature has little effect on the frequency response of the actuator, the first resonant frequency is kept at 1270 Hz, the change of which is less than 0.17% within 70 °C, and the bandwidth can all exceed 2000 Hz.
(4) The proposed analytical model can accurately describe the temperature-dependent characteristics of the multidimensional discrete magnetostrictive actuator, the root mean square error of which is less than 3% within 200 Hz and less than 7.4% at 400 Hz.

Declaration of competing interest

The authors declare that they have no known competing financial interests or personal relationships that could have appeared to influence the work reported in this paper.

Data availability

Data will be made available on request.

Appendix A

The temperature-dependent magnetic equivalent circuit model of the MDMA can be calculated as [24]:

$$\begin{cases} \phi_7+\phi_{10}-\phi_4=0,\ \phi_1+\phi_5+\phi_6-\phi_{10}=0 \\ \phi_2+\phi_8+\phi_9-\phi_5-\phi_6=0,\ \phi_3-\phi_8-\phi_9=0 \\ \phi_{11}+\phi_{15}-\phi_1=0,\ \phi_{13}-\phi_3-\phi_{12}=0 \\ \phi_{12}+\phi_{14}-\phi_2-\phi_{11}=0 \\ \phi_4(R_{\text{shell}}+R_{\text{m}}+R_{\text{pm}})+\phi_7R_L-NI-F_{\text{pm}}^T=0 \\ \phi_{10}R_{\text{base}}+\phi_1R_{\text{rod1}}^{M,T,\sigma}+\phi_{15}(R_{\text{s12}}+R_{\text{AG3}})-\phi_7R_L=0 \\ \phi_5R_1+\phi_2R_{\text{rod2}}^{M,T,\sigma}-\phi_1R_{\text{rod1}}^{M,T,\sigma}-\phi_{11}R_3=0 \\ \phi_3R_{\text{rod3}}^{M,T,\sigma}+\phi_9R_2-\phi_2R_{\text{rod2}}^{M,T,\sigma}-\phi_{12}R_4=0 \\ \phi_{11}R_3+\phi_{14}(R_{\text{s22}}+R_{\text{AG4}})-\phi_{15}(R_{\text{s12}}+R_{\text{AG3}})=0 \\ \phi_{12}R_4+\phi_{13}R_{\text{or}}-\phi_{14}(R_{\text{s22}}+R_{\text{AG4}})=0 \\ \phi_8(R_{\text{s21}}+R_{\text{AG2}})-\phi_9R_2=0 \\ \phi_6(R_{\text{s11}}+R_{\text{AG1}})-\phi_5R_1=0 \end{cases} \tag{23}$$

where NI is the excitation magnetomotive force; R_{shell}, R_{or}, R_{base}, R_{m} and R_{pm} are the magnetic reluctance of the inner shell, output rod, base, iron rings and permanent magnets respectively; R_{s11}, R_{s12}, R_{s21} and R_{s22} are the magnetic reluctance of magnetizer 2, magnetizer 1, magnetizer 4 and magnetizer 3 respectively; R_{L} is the leakage magnetic reluctance; R_{AG1} to R_{AG4} are the air gaps magnetic reluctance; R_1 to R_4 are the radial transfer magnetic reluctance; ϕ_1 to ϕ_{15} are the magnetic flux of each branch in the TDMEC model.

Appendix B

The mass matrix $\boldsymbol{M}$, the damping matrix $\boldsymbol{C}$, the displacement matrix $\boldsymbol{X}$ and the input force matrix $\boldsymbol{F}$ in the multi-body mechanical dynamic model can be expressed as [40]:

$$\boldsymbol{M}=\begin{bmatrix} \frac{m_1}{3}+m_{\text{lr1}} & 0 & 0 \\ 0 & \frac{m_2}{3}+m_{\text{lr2}} & 0 \\ 0 & 0 & \frac{m_3}{3}+m_{\text{lr3}} \end{bmatrix} \tag{24}$$

$$\boldsymbol{C}=\begin{bmatrix} c_1+c_{\text{lr1}} & 0 & 0 \\ 0 & c_2+c_{\text{lr2}} & 0 \\ 0 & 0 & c_3+c_{\text{lr3}} \end{bmatrix} \tag{25}$$

$$\boldsymbol{X}=\begin{bmatrix} x_1 \\ x_2 \\ x_3 \end{bmatrix},\ \boldsymbol{F}=\begin{bmatrix} F_1 \\ F_2 \\ F_3 \end{bmatrix} \tag{26}$$

where m_1, m_2 and m_3 are the masses of rod 1, rod 2 and rod 3 respectively; c_1, c_2 and c_3 are the damping of rod 1, rod 2 and rod 3 respectively; x_1, x_2 and x_3 are the output displacement of rod 1, rod 2 and rod 3 respectively; F_1, F_2 and F_3 are the output force of rod 1, rod 2 and rod 3 respectively; m_{lr1}, m_{lr2} and m_{lr3} are the equivalent load mass of rod 1, rod 2 and rod 3 respectively; c_{lr1}, c_{lr2} and c_{lr3} are the equivalent load damping of rod 1, rod 2 and rod 3 respectively. This can be described as:

$$\begin{cases} m_{\text{lr1}}=m_{\text{M1}}+m_{\text{t1}}+m_{\text{M2}}+m_2+m_{\text{M3}} \\ \qquad +m_{\text{t2}}+m_{\text{M4}}+m_3+m_{\text{s}} \\ m_{\text{lr2}}=m_{\text{M3}}+m_{\text{t2}}+m_{\text{M4}}+m_3+m_{\text{s}} \\ m_{\text{lr3}}=m_{\text{s}} \end{cases} \tag{27}$$

$$\begin{cases} c_{\text{lr1}}=(\frac{1}{c_{\text{M1}}}+\frac{1}{c_{\text{t1}}}+\frac{1}{c_{\text{M2}}}+\frac{1}{c_2}+\frac{1}{c_{\text{M3}}} \\ \qquad +\frac{1}{c_{\text{t2}}}+\frac{1}{c_{\text{M4}}}+\frac{1}{c_3}+\frac{1}{c_{\text{s}}}+\frac{1}{c_{\text{dh}}})^{-1} \\ c_{\text{lr2}}=(\frac{1}{c_{\text{M3}}}+\frac{1}{c_{\text{t2}}}+\frac{1}{c_{\text{M4}}}+\frac{1}{c_3}+\frac{1}{c_{\text{s}}}+\frac{1}{c_{\text{dh}}})^{-1} \\ c_{\text{lr3}}=(\frac{1}{c_{\text{s}}}+\frac{1}{c_{\text{dh}}})^{-1} \end{cases} \tag{28}$$

where m_{M1}, m_{t1}, m_{M2}, m_{M3}, m_{t2}, m_{M4} and m_s are the mass of magnetizer 1, sleeve 1, magnetizer 2, magnetizer 3, sleeve 2, magnetizer 4, and output rod respectively; c_{M1}, c_{t1}, c_{M2}, c_{M3}, c_{t2}, c_{M4}, c_s and c_{dh} are the damping of magnetizer 1, sleeve 1, magnetizer 2, magnetizer 3, sleeve 2, magnetizer 4, output rod and disk spring respectively.

References

[1] L. Li, Y. Lin, Z. Fu, C. Zhang, Emission characteristics of a model combustor for aero gas turbine application, Exp. Therm Fluid Sci. 72 (2016) 235–248.

[2] Z. Sun, M. Cui, C. Ye, S. Yang, X. Li, D. Hung, M. Xu, Split injection flash boiling spray for high efficiency and low emissions in a GDI engine under lean combustion condition, Proc. Combust. Inst. 38 (4) (2021) 5769–5779.

[3] V. Sethi, X. Sun, D. Nalianda, A. Rolt, P. Holborn, C. Wijesinghe, C. Xisto, I. Jonsson, T. Grönstedt, J. Ingram, et al., Enabling cryogenic hydrogen-based CO 2-free air transport: Meeting the demands of zero carbon aviation, IEEE Electrif. Mag. 10 (2) (2022) 69–81.

[4] X. Han, D. Laera, A.S. Morgans, Y. Lin, C. Zhang, X. Hui, C.J. Sung, Inlet temperature driven supercritical bifurcation of combustion instabilities in a lean premixed prevaporized combustor, Exp. Therm Fluid Sci. 109 (2019) 109857.

[5] C. Ruan, F. Chen, T. Yu, W. Cai, Y. Mao, Y. Qian, X. Li, X. Lu, Experimental study on combustion stability characteristics in liquid-fueled gas turbine model combustor: Fuel sensitivities and flame/flow dynamics, Fuel 265 (2020) 116973.

[6] Y. Cheng, T. Jin, K. Luo, Z. Li, H. Wang, J. Fan, Large eddy simulations of spray combustion instability in an aero-engine combustor at elevated temperature and pressure, Aerosp. Sci. Technol. 108 (2021) 106329.

[7] T. Poinsot, Prediction and control of combustion instabilities in real engines, Proc. Combust. Inst. 36 (1) (2017) 1–28.

[8] T. Indlekofer, B. Ahn, Y.H. Kwah, S. Wiseman, M. Mazur, J.R. Dawson, N.A. Worth, The effect of hydrogen addition on the amplitude and harmonic response of azimuthal instabilities in a pressurized annular combustor, Combust. Flame 228 (2021) 375–387.

[9] A. Morgans, A. Dowling, Model-based control of combustion instabilities, J. Sound Vib. 299 (1) (2007) 261–282.

[10] D. Zhao, Z. Lu, H. Zhao, X. Li, B. Wang, P. Liu, A review of active control approaches in stabilizing combustion systems in aerospace industry, Prog. Aerosp. Sci. 97 (2018) 35–60.

[11] S. Tachibana, L. Zimmer, Y. Kurosawa, K. Suzuki, Active control of combustion oscillations in a lean premixed combustor by secondary fuel injection coupling with chemiluminescence imaging technique, Proc. Combust. Inst. 31 (2) (2007) 3225–3233.

[12] J.P. Hathout, M. Fleifil, A.M. Annaswamy, A.F. Ghoniem, Combustion instability active control using periodic fuel injection, J. Propuls. Power 18 (2) (2002) 390–399.

[13] C. Hantschk, J. Hermann, D. Vortmeyer, Active instability control with direct-drive servo valves in liquid-fueled combustion systems, Symp. (Int.) Combust. 26 (2) (1996) 2835–2841.

[14] N. Docquier, S. Candel, Combustion control and sensors: a review, Prog. Energy Combust. Sci. 28 (2) (2002) 107–150.

[15] Y. Liu, J. Li, T. Zhang, Y. Yan, Active suppression of swirl-stabilized combustion instability, Fuel 287 (2021) 119559.

[16] S. Feng, J. Li, H loop-shaping control of azimuthal combustion instabilities in annular combustors, J. Low Freq. Noise Vib. Act. Control 40 (1) (2021) 395–412.

[17] J. Rubio-Hervas, M. Reyhanoglu, W. MacKunis, Observer-based sliding mode control of Rijke-type combustion instability, J. Low Freq. Noise Vib. Act. Control 34 (2) (2015) 201–217.

[18] J. DeLaat, K. Breisacher, J. Saus, D. Paxson, Active combustion control for aircraft gas turbine engines, in: 36th AIAA/ASME/SAE/ASEE Joint Propulsion Conference and Exhibit, 2000, p. 3500.

[19] N.H. Schiller, W.R. Saunders, W.A. Chishty, U. Vandsburger, W.T. Baumann, Development of a piezoelectric-actuated fuel modulation system for active combustion control, J. Intell. Mater. Syst. Struct. 17 (5) (2006) 403–410.

[20] H. Nabae, T. Higuchi, A novel electromagnetic actuator based on displacement amplification mechanism, IEEE/ASME Trans. Mechatronics 20 (4) (2015) 1607–1615.

[21] G. Xue, P. Zhang, X. Li, Z. He, H. Wang, Y. Li, R. Ce, W. Zeng, B. Li, A review of giant magnetostrictive injector (GMI), Sensors Actuators A 273 (2018) 159–181.

[22] J.L. Chen, C.L. Zhang, M.L. Xu, Y.Y. Zi, X.N. Zhang, Rhombic micro-displacement amplifier for piezoelectric actuator and its linear and hybrid model, Mech. Syst. Signal Process. 50–51 (2015) 580–593.

[23] Y. Tian, K. Lu, F. Wang, C. Zhou, Y. Ma, X. Jing, C. Yang, D. Zhang, A spatial deployable three-DOF compliant nano-positioner with a three-stage motion amplification mechanism, IEEE/ASME Trans. Mechatronics 25 (3) (2020) 1322–1334.

[24] L. Chen, Y. Zhu, J. Ling, M. Zhang, Development and characteristic investigation of a multidimensional discrete magnetostrictive actuator, IEEE/ASME Trans. Mechatronics 27 (4) (2022) 2071–2079.

[25] K. Jin, Y. Kou, X. Zheng, A nonlinear magneto-thermo-elastic coupled hysteretic constitutive model for magnetostrictive alloys, J. Magn. Magn. Mater. 324 (12) (2012) 1954–1961.

[26] Y.S. Zhan, C.h. Lin, A constitutive model of coupled magneto-thermo-mechanical hysteresis behavior for giant magnetostrictive materials, Mech. Mater. 148 (2020) 103477.

[27] A. Raghunathan, Y. Melikhov, J.E. Snyder, D. Jiles, Theoretical model of temperature dependence of hysteresis based on mean field theory, IEEE Trans. Magn. 46 (6) (2010) 1507–1510.

[28] H.M. Zhou, M.H. Li, X.H. Li, D.G. Zhang, An analytical and explicit multi-field coupled nonlinear constitutive model for Terfenol-D giant magnetostrictive material, Smart Mater. Struct. 25 (8) (2016) 085036.

[29] W. Huang, Z. Xia, P. Guo, L. Weng, Analysis and experimental research on high frequency magnetic properties of different magnetostrictive materials under variable temperature conditions, AIP Adv. 12 (3) (2022) 035231.

[30] D. Poker, C. Klabunde, Temperature dependence of electrical resistivity of vanadium, platinum, and copper, Phys. Rev. B 26 (12) (1982) 7012.

[31] B. Cook, J. Harringa, T. Hansen, Electrical and thermal properties of Tb 0.3 Dy 0.7 Fe 2- x, J. Appl. Phys. 87 (2) (2000) 776–780.

[32] M. Fukuhara, A. Sanpei, Elastic moduli and internal friction of low carbon and stainless steels as a function of temperature, ISIJ Int. 33 (4) (1993) 508–512.

[33] S. Münstermann, Y. Feng, W. Bleck, Influencing parameters on elastic modulus of steels, Can. Metall. Q. 53 (3) (2014) 264–273.

[34] L. Zhou, R. Hall, C. Davis, Measured and modelled low field relative permeability for dual phase steels at high temperature, J. Magn. Magn. Mater. 475 (2019) 38–43.

[35] Z. Wang, K.y. He, J. Jin, J. He, L. Zhang, H.w. Zhang, B.g. Shen, Temperature dependence of permeability for Fe–Cu–M–Si–B alloys, Mater. Sci. Eng. A 304 (2001) 1046–1049.

[36] W. Cai, P. Feng, J. Zhang, Z. Wu, D. Yu, Effect of temperature on the performance of a giant magnetostrictive ultrasonic transducer, J. Vibroengineering 18 (2) (2016) 1307–1318.

[37] W. Huang, Z. Deng, M.J. Dapino, L. Weng, B. Wang, Electromagnetic-mechanical-thermal fully coupled model for Terfenol-D devices, J. Appl. Phys. 117 (17) (2015) 17A915.

[38] S. Yi, Q. Zhang, L. Xu, T. Wang, L. Li, Hysteresis online identification approach for smart material actuators with different input signals and external disturbances, Nonlinear Dynam. (2022).

[39] Y.C. Zhu, X.L. Yang, N.M. Wereley, Research on hysteresis loop considering the prestress effect and electrical input dynamics for a giant magnetostrictive actuator, Smart Mater. Struct. 25 (8) (2016).

[40] L. Chen, Y. Zhu, J. Ling, Z. Feng, Theoretical modeling and experimental evaluation of a magnetostrictive actuator with radial-nested stacked configuration, Nonlinear Dynam. 109 (3) (2022) 1277–1293.

[41] J. Blázquez, V. Franco, A. Conde, L. Kiss, Soft magnetic properties of high-temperature nanocrystalline alloys: Permeability and magnetoimpedance, J. Appl. Phys. 93 (4) (2003) 2172–2177.

[42] P. Zhou, D. Lin, Y. Xiao, N. Lambert, M.A. Rahman, Temperature-dependent demagnetization model of permanent magnets for finite element analysis, IEEE Trans. Magn. 48 (2) (2012) 1031–1034.

[43] D. Jiles, D. Atherton, Theory of ferromagnetic hysteresis, J. Magn. Magn. Mater. 61 (1) (1986) 48–60.

[44] L. Sun, X. Zheng, Numerical simulation on coupling behavior of Terfenol-D rods, Int. J. Solids Struct. 43 (6) (2006) 1613–1623.

[45] X. Sun, B. Yang, W. Hu, Z. Bai, Simultaneous precision positioning and vibration control for on-orbit optical payloads: an integrated actuator development and analysis, J. Vib. Eng. Technol. 9 (4) (2021) 507–528.

[46] Y. Zhu, Y. Li, A hysteresis nonlinear model of giant magnetostrictive transducer, J. Intell. Mater. Syst. Struct. 26 (16) (2015) 2242–2255.

[47] J.R. Saus, R. Thomas, An overview of high bandwidth liquid fuel flow modulators developed for active combustion control research, 2018.